WHITE PAPER

THE COST OF FUTURE COLLISIONS IN LEO

Eugene M. Levin* **and Joseph A. Carroll†**

*Star Technology and Research, Inc., USA
†Tether Applications, Inc., USA

February 28, 2012

Executive Summary

As debris mitigation practices improve, catastrophic collisions involving large debris objects can become the dominant source of debris pollution in low Earth orbits. These collisions will produce hundreds of thousands of debris fragments in the centimeter range ("shrapnel") that are hard to track, but could be lethal to operational spacecraft.

There are non-trivial costs associated with catastrophic collisions and their consequences, some of them not immediately obvious. Our primary goal was to find a way to calculate the average statistically expected loss of assets after a catastrophic collision in a transparent and compact manner. We want it to be suitable for direct parametric analysis by decision makers, the space insurance industry, and the scientific community alike.

We did not rely on the existing fragmentation models, because they still need to be updated based on the latest on-orbit collision data. Instead, we used the two most relevant empirical data points, the Fengyun-1C and Cosmos-Iridium events, to develop a high-level phenomenological model of production, distribution, and accumulation of small but lethal fragments in catastrophic collisions. The model is statistical and operates with mass distributions and virtual fluxes of debris fragments. It allows analytical evaluation of the statistically expected damage to operational satellites from future collisions in LEO.

Using this model, we have found that the primary loss occurs not in the catastrophic collision itself, but within a decade after the collision, when a piece of untracked "shrapnel" produced in that collision hits a high value asset. It could be a "hidden" loss, because it may be hard to determine the true reason for the asset failure.

We believe that the production of "shrapnel" and its long-term impact on the LEO environment are usually underestimated. The existing focus is biased toward trackable fragments over 10 cm. The average expected rate of production of lethal but untracked "shrapnel" will continue to grow with new launches, and will remain substantial until wholesale removal is achieved. The fragment yield of an average catastrophic collision is likely to exceed the yield of the Fengyun-1C and Cosmos–Iridium events combined. Removal of a few large debris objects per year would not reduce the rate and fragment yield of catastrophic collisions in LEO enough to prevent accumulation of "shrapnel" at altitudes above 800 km, where it will persist for a very long time.

Our model clearly shows how different debris removal campaigns would affect average statistically expected production of "shrapnel" in LEO and why wholesale removal of large debris is necessary for restoring the LEO environment.

We also suggest that most "shrapnel" may be produced by "hypervelocity sprays" shredding those parts of colliding objects that missed the direct impact.

CONTENTS

1. Introduction

It is now recognized that a single catastrophic collision between intact objects in LEO can negate many years of debris mitigation efforts. We will see below that an average catastrophic collision is likely to be on the scale of the Fengyun-1C and Cosmos–Iridium events combined. They produced on the order of 400,000 fragments in the centimeter range ("shrapnel"), an amount comparable to the accumulation of explosion fragments over 50 years of spaceflight. These fragments are currently untracked and impossible to avoid, but they can disable or seriously damage operational satellites. The full extent of LEO pollution resulting from five decades of space activities and various unplanned events will be more obvious when small fragments become trackable with new observation techniques in the future. In this new world, the everyday task of collision avoidance will be much more difficult due to the sheer number of objects to avoid, and the task of debris removal will look much more urgent.

In order to prevent further LEO pollution with more fragments produced in catastrophic collisions, large debris objects, the primary source of future "shrapnel," should be removed from densely populated regions in LEO [1,2,3]. There is a range of opinions on how many objects should be removed annually. NASA has been conservatively suggesting removal of five large objects per year [1], assuming 90% post-mission disposal compliance, while ESA has indicated that there may be a need to remove up to 27 objects per year in some scenarios [2]. These campaigns would be long-term in nature, and it would take a very long time to get rid of the 2,200 large debris objects currently in low Earth orbits. During this time, catastrophic collisions and production of "shrapnel" will continue. The authors of this paper recently argued in favor of a short-term wholesale debris removal campaign [3], in which electrodynamic "garbage trucks" of the latest design could remove several hundred objects per year at a very reasonable cost, and LEO could be mostly free of large debris objects in a decade or so. In this scenario, catastrophic collisions will become very unlikely, and practically no more "shrapnel" will be produced.

Before decisions can be made on debris removal campaigns, we need to better understand and evaluate the potential impact of future catastrophic collisions on operational spacecraft. One of the pioneering studies in this area was undertaken by the Aerospace Corporation [4]. The study evaluated added costs of operating three types of constellations in a gradually deteriorating LEO environment. The existing models of the LEO debris environment, such as ORDEM, MASTER, and others, could be used for such evaluations, however, they are rather complex due to the level of detail and not easy to apply in analytical studies. In addition, their implementations are numeric, and details of these implementations are not publicly available. In this paper, we formulate a relatively simple analytical model and apply it to the evaluation of the cost of future collisions in LEO.

We will not rely on the existing fragmentation models, because we expect them to be updated based on the latest on-orbit collision data. Instead, we will use the two most relevant empirical data points, the Fengyun-1C and Cosmos-Iridium events, to develop a high-level phenomenological model of production and accumulation of small but lethal fragments in catastrophic collisions. While it is more common these days to use size distributions, we will use mass distributions of fragments to estimate the loss of assets, because damage is determined not so much by the size, but by the mass of a fragment hitting the asset. Several "tunable" parameters will be introduced. We will point out their likely values, but these values can be easily adjusted as more data becomes available.

2. Future catastrophic collisions

Let us consider a set of objects $\{B_k\}$ large enough to cause catastrophic collisions with spacecraft and upper stages in LEO. This set includes operational spacecraft as a subset $\{A_n\}$. To evaluate the statistical impact of future catastrophic collisions and quantify the difference between removing and not removing large debris objects, we will exclude all small debris fragments currently in orbit from calculations. They represent the background risk that already exists and does not depend on the future removal of large debris. The risk of damage to the assets A_n has two components that strongly depend on the persistence of large debris: a) the assets can collide with one of the objects B_k, and b) they can be hit by fragments generated in future catastrophic collisions between the objects B_k. Fig. 1 illustrates these two possibilities. The damage of the first kind is done immediately by the collision, while the damage of the second kind is delayed and may not even be identified as debris-related when it occurs.

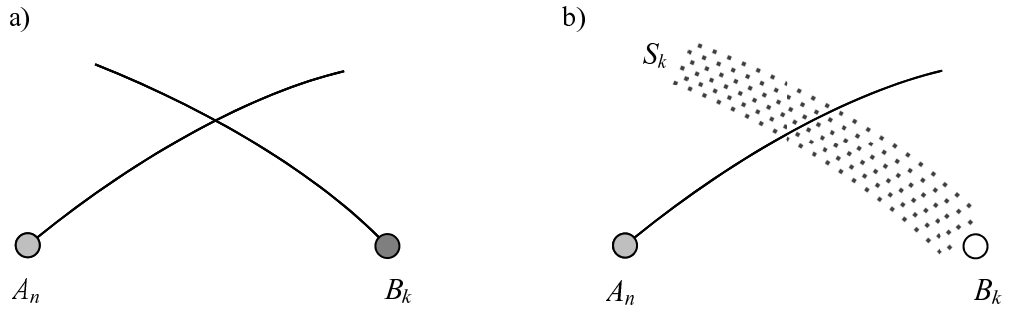

Fig. 1. Collisions with objects (a) and their fragments (b).

The orbits of LEO objects are evolving with time, and there are many inherent uncertainties in their evolution, making predictions difficult and not very reliable. Instead of simulating the long-term evolution, we suggest looking at statistical snapshots derived from the current state at any given time in order to understand the developing trends.

We start by calculating the annual probabilities P_{ij} of collisions between objects B_i and B_j based on averaging over a representative period of time. A method developed by Kessler [5] can be applied to this calculation, as well as other approaches. For the purposes of this article, we will use a simplified method described in Appendix A. The values P_{ij} are rather small, and we will retain only linear terms in the cumulative probability calculations.

The annual probability of a catastrophic collision is calculated as

$$P_c = \sum_{i<j} P_{ij}, \tag{1}$$

while the annual probability that an object B_k will be involved in a catastrophic collision is given by

$$P_k = \sum_i P_{ki}. \tag{2}$$

If the object successfully maneuvers to avoid tracked objects, all values P_{ki} can be set to 0, resulting in $P_k = 0$. However, untracked objects cannot be avoided.

The average statistically expected yield of fragments in a catastrophic collision in terms of mass is calculated as

$$M_f = \frac{1}{P_c} \sum_{i<j} (M_i + M_j)\, P_{ij} = \frac{1}{P_c} \sum_k M_k P_k, \tag{3}$$

where M_k are the masses of the objects B_k. In the current LEO debris field, the average yield is about 2.7 tons, which is more than the yield of the Fengyun-1C and Cosmos-Iridium events combined. Fig. 2 shows the distribution of the expected fragment yields by 1-ton ranges. The last bar covers the range from 10 to 17 tons. We see that the Cosmos-Iridium collision was on the small side. Over 60% of the catastrophic collisions will yield more than 2 tons of fragments.

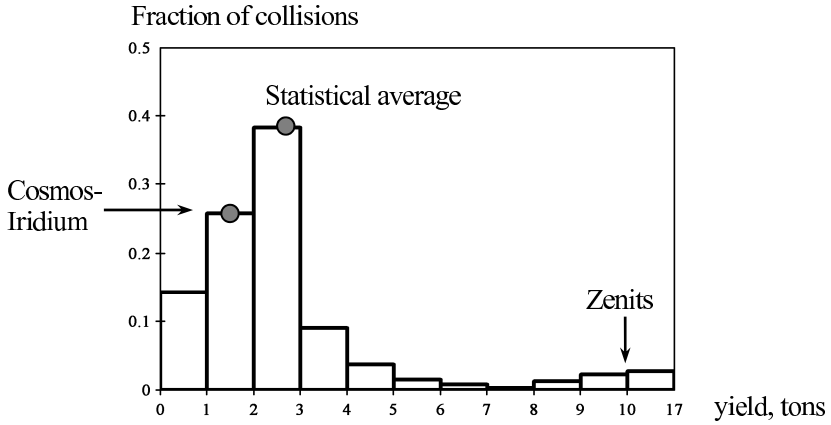

Fig. 2. Distribution of the yield of fragments.

Judging by the number of small fragments produced in the Fengyun-1C and Cosmos-Iridium events (see Appendix B), we can expect on the order of half a million "shrapnel" pieces in the centimeter range to be released in an average catastrophic collision. Collision fragments form streams centered around the orbits of the originating objects, and with time, their nodes spread due to the differential nodal regression, forming shells around the Earth and creating substantial additional risk to the operational satellites. This risk can be expressed in terms of the average statistically expected damage to the assets in LEO. We will use a concept of a virtual stream of collision fragments for this purpose.

3. Virtual streams of collision fragments

Let us consider a phase space where the semi-major axes, eccentricities and inclinations of the orbits of the objects B_k are set at their current values, but other parameters are randomly distributed. For each pair of objects B_k and B_i, we look at all possible collision geometries and derive an average distribution $\rho_{ki}(m, H)$ describing mean statistical properties of the stream of fragments of the object B_k expected to be produced in a collision with the object B_i, where

$$dN = \rho_{ki}(m, H)\, dm\, dH$$

is the average number of fragments with masses between m and $m + dm$ expected to be found at altitudes between H and $H + dH$. Keeping in mind that some fragments will be reentering shortly after collisions, the total mass of the fragments will be less or equal to the original mass M_k of the object B_k,

$$\int_0^\infty \int_0^\infty m\, \rho_{ki}(m, H)\, dm\, dH \leqslant M_k. \tag{4}$$

The average statistically expected distribution of fragments of the object B_k generated in a possible collision with another object can be calculated as

$$\rho_k(m, H) = \frac{1}{P_k} \sum_i P_{ki}\, \rho_{ki}(m, H), \tag{5}$$

where P_k is the the annual probability (2) of a collision involving the object B_k. The total statistically expected stream of fragments produced in a catastrophic collision can be characterized by the following distribution

$$\rho_c(m, H) = \frac{1}{P_c} \sum_{i<j} (\rho_{ij} + \rho_{ji})\, P_{ij} = \frac{1}{P_c} \sum_k P_k\, \rho_k(m, H), \tag{6}$$

where P_c is the annual probability of a catastrophic collision (1). The streams of fragments characterized by distribution (5) and (6) are virtual, because they

are synthesized from the probability-weighted and time-averaged streams from all possible catastrophic collisions. However, we can treat them as physical streams for the purpose of statistical damage calculations.

We will now focus on a very narrow range of fragment masses around 1 g that are believed to be at the "threshold of lethality" in terms of the impacts on the operational satellites. For short-term projections in this range, we will separate mass and altitude distributions by setting

$$\rho_{ki}(m,H) = f_{ki}(m)\, g_{ki}(H). \tag{7}$$

We will also use cumulative distributions

$$F_{ki}(m) = \int_m^\infty f_{ki}(\mu)\, d\mu \tag{8}$$

and

$$G_{ki}(H) = \int_H^\infty g_{ki}(h)\, dh. \tag{9}$$

Appendix B suggests a simple power law distribution for the number of fragments heavier than m,

$$F_{ki}(m) = \varkappa_{ki} M_k\, (m_c/m)^\gamma, \tag{10}$$

where $m_c = 1$ g is a characteristic mass, $\varkappa_{ki}$ is the average statistically expected yield of fragments heavier than m_c per unit mass of the object B_k produced in a collision with the object B_i, M_k is the mass of the object B_k, and $\gamma \approx 0.8$. Based on the data from the Fengyun-1C and Cosmos-Iridium events, an estimate of $\varkappa_{ki} \approx 24/\text{kg}$ is derived in Appendix B. For each object, the average yield will depend on its composition and design. The corresponding distribution density is

$$f_{ki}(m) = \varkappa_{ki} M_k \gamma\, m_c^\gamma / m^{\gamma+1}. \tag{11}$$

Analysis in Appendix C suggests the following approximation for the altitude distribution of collision fragments

$$n(h,h_0) = \frac{k_0}{h_s} \left(1 + \frac{|h-h_0|}{h_s}\right)^{-b}, \tag{12}$$

where h_0 is the collision altitude, h_s is the scale height of the distribution, $b \approx 2.37$, and $k_0 = (b-1)/2 \approx 0.69$ is a normalization coefficient, such that

$$\int_0^\infty n(h,h_0)\, dh = 1.$$

Characteristic values of h_s are estimated in Appendix C for tracked collision fragments, however, there is no data on small untracked fragments. It is anticipated

that their altitude distributions should be wider, and we will use values ∼150 km for fragments ∼1 g. Calculations show that the overall results do not change much within a reasonable range of h_s.

Each object B_k moves between its perigee H_{pk} and apogee H_{ak}. With a relatively small eccentricity, typical in LEO, the altitude residence density according to the laws of Kepler's motion can be approximated as

$$r_k(h) \approx \frac{1}{\pi\sqrt{(H_{ak}-h)(h-H_{pk})}}. \tag{13}$$

The altitude residence density $r_i(H)$ of another object B_i is similarly distributed between its perigee H_{pi} and apogee H_{ai}. If these altitude ranges overlap, the two objects can collide at some altitude h_0 within the overlapping range (h_1, h_2). Then, the probability-weighted altitude distribution of the virtual stream of fragments from all possible collisions between the two objects is obtained by integration

$$g_{ki}(H) = \frac{1}{R_{ki}} \int_{h_1}^{h_2} n(H, h_0)\, r_k(h_0)\, r_i(h_0)\, dh_0, \tag{14}$$

where $n(H, h_0)$ is defined by (12), and the normalization coefficient is

$$R_{ki} = \int_{h_1}^{h_2} r_k(h_0)\, r_i(h_0)\, dh_0.$$

The corresponding cumulative distribution (9) is calculated as

$$G_{ki}(H) = \frac{1}{R_{ki}} \int_{h_1}^{h_2} N(H, h_0)\, r_k(h_0)\, r_i(h_0)\, dh_0, \tag{15}$$

where $N(h, h_0)$ is the cumulative distribution for the density (12)

$$N(h, h_0) = \begin{cases} (1 + |h - h_0|/h_s)^{1-b}/2 & \text{with } \ h \geqslant h_0, \\ 1 - (1 + |h - h_0|/h_s)^{1-b}/2 & \text{with } \ h < h_0. \end{cases} \tag{16}$$

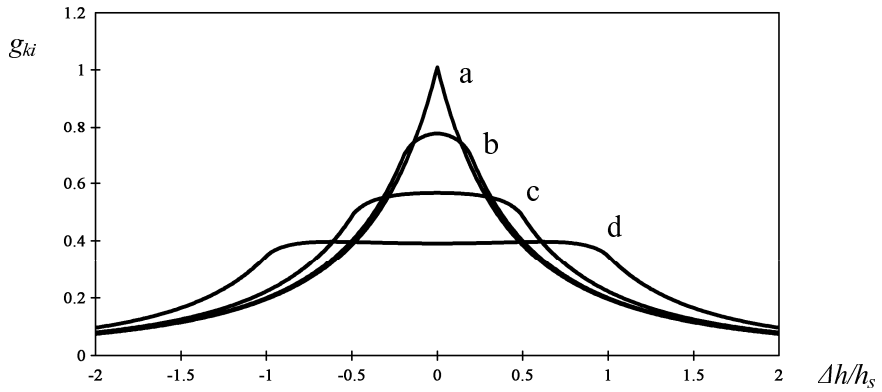

Fig. 3. Altitude profile of the virtual flux depending on the eccentricity: a) $e = 0$, b) $e = 0.2h_s/R$, c) $e = 0.5h_s/R$, d) $e = h_s/R$.

Fig. 3 shows how the distribution (14) widens with the eccentricity in case when the altitude range of the object B_k is substantially narrower than the altitude range of the object B_i. This example is equivalent to setting $r_i \approx const$ and is given for illustrative purposes. All profiles are shown relative to the peak value with $e = 0$.

As more observation data on small fragments becomes available, the model can be updated as needed.

4. Virtual flux at a given inclination

According to formulas (5)–(7), the average statistically expected stream of fragments from a catastrophic collision can be characterized by the following distribution

$$\rho_c = \sum_k S_k, \qquad S_k = \frac{1}{P_c} \sum_i P_{ki}\, f_{ki}(m)\, g_{ki}(H). \tag{17}$$

It represents a superposition of the individual sub-streams S_k of the future collision fragments of the objects B_k. The orbits of the fragments in each sub-stream S_k will have inclinations close to the inclination i_k of the originating object B_k, but their ascending nodes will be widely dispersed due to the nodal regression and statistical averaging over all possible realizations of the collision process. When an asset A_n crosses paths with a fragment F_k from a sub-stream S_k, the probability of a hit will depend on the conjunction geometry, and in particular, on the angle α_{nk} between their trajectories at the conjunction point (Fig. 4).

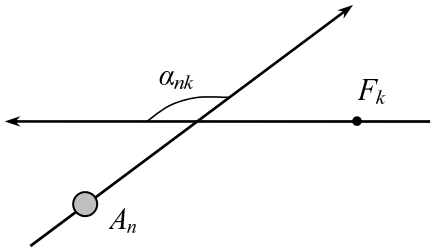

Fig. 4. Conjunction geometry.

To evaluate the virtual flux encountered by the assets at different inclinations, let us consider a sphere of radius r_n moving in a circular orbit of radius R_n (altitude H_n) at an inclination i_n. The average number of fragments of the virtual stream (17) heavier than m found in the spherical layer $(R_n - r_n, R_n + r_n)$ is calculated as

$$N_r = \sum_k N_{rk}, \qquad N_{rk} = 2r_n \int_m^\infty S_k(\mu, H_n)\, d\mu. \tag{18}$$

The fragments generally move in elliptic orbits, entering and leaving the spherical layer, but the counts N_{rk} are maintained on average. To estimate the number

of hits on the sphere, we will consider an equivalent flux of fragments moving in circular orbits with random nodes and random phasing in the layer $(R_n - r_n, R_n + r_n)$. In this formulation, each fragment will cross the orbit of the sphere two times per orbit. Using the method described in Appendix A and integrating over the cross-section, the average probability of a hit by a fragment from a sub-stream S_k at any given crossing is estimated as

$$P_{\beta k} \approx \frac{r_n \beta_{nk}}{4R_n}, \tag{19}$$

where

$$\beta_{nk} = \frac{1}{2\pi} \int_0^{2\pi} \frac{d\varphi_{nk}}{\cos(\alpha_{nk}/2)}, \tag{20}$$

and the averaging takes place over the ascending node differences φ_{nk} between the orbit of the sphere and the fragments from the virtual sub-stream S_k.

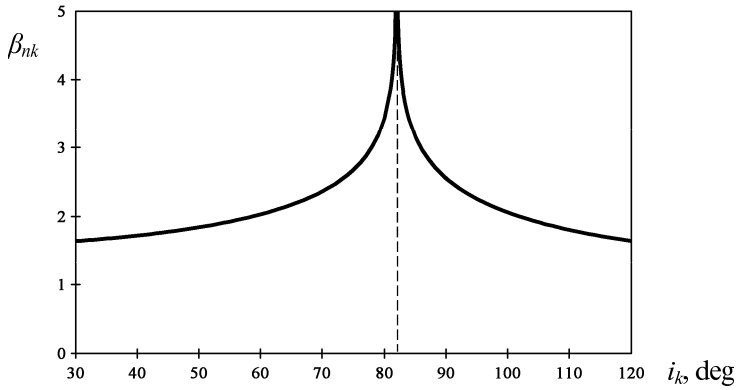

Fig. 5. "Inclination pairing" coefficient for sun-sync objects.

The multipliers β_{nk} reflect what Carroll called "inclination pairing" [6]. They peak when $i_n + i_k$ approaches 180°. It means, in particular, that sun-sync assets will be strongly "paired" with the future fragments of the objects from the 81–83° cluster, as illustrated in Fig. 5. This happens because their orbits precess in the opposite directions, and when they become nearly coplanar, the objects and fragments move head-on, greatly increasing the probability of a hit.

The total number of fragments of the virtual sub-stream S_k hitting the test sphere every orbit will be $2N_{rk}P_{\beta k}$. Dividing this number by the collision cross-section area of the sphere πr_n^2 and by the orbital period $2\pi/\omega_n$, where ω_n is the angular rate of the orbital motion, and performing summation over all sub-streams, we find that the average virtual flux of future collision fragments heavier than m encountered by an asset A_n orbiting at an inclination i_n can be approximated as

$$\Phi_n \approx \frac{k_n}{P_c} \sum_{k,i} \beta_{nk}\, P_{ki}\, F_{ki}(m)\, g_{ki}(H_n). \tag{21}$$

where $F_{ki}(m)$ is the cumulative distribution (8), H_n is the average altitude of the asset A_n, and

$$k_n = \frac{\omega_n}{2\pi^2 R_n}.$$

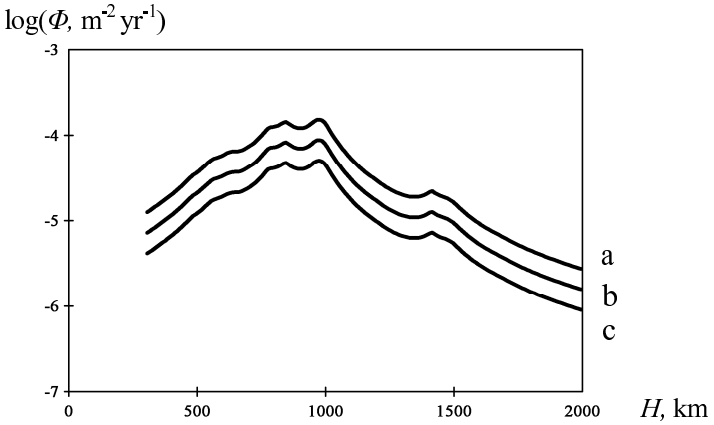

Fig. 6. Post-collision increase of the debris flux on sun-sync assets: a) $m > 0.5$ g, b) $m > 1$ g, c) $m > 2$ g.

The flux of fragments with masses between m and $m + dm$ is calculated as $\Psi_n dm$, where

$$\Psi_n \approx \frac{k_n}{P_c} \sum_{k,i} \beta_{nk}\, P_{ki}\, f_{ki}(m)\, g_{ki}(H_n). \tag{22}$$

Formulas (17) and (21) characterize the current state of the LEO debris field in terms of the average statistically expected production of small fragments in a catastrophic collision between large objects. Fig. 6 shows how the fluxes on sun-sync assets will increase on average in three different fragment mass ranges after a catastrophic collision. The virtual fluxes peak around 900 km, because this is where the primary sources of the future fragments are concentrated.

It is interesting to note that a fairly accurate approximation for the overall flux can be obtained by replacing the weighted distributions (14) in formulas (21)–(22) with the base distributions (12) centered around the middle of the altitude overlap. It works because the altitude overlaps are typically small compared to the scale heights of the altitude distributions, and because the number of objects is large.

5. The cost of a catastrophic collision

The cost of a catastrophic collision includes an immediate loss, if an asset was destroyed in the collision, and a delayed loss, if other assets were damaged later

by the fragments produced in the collision. The average statistically expected immediate loss caused by a catastrophic collision can be evaluated as

$$L_c = \frac{1}{P_c} \sum_{i<j} (L_i + L_j)\, P_{ij} = \frac{1}{P_c} \sum_k L_k P_k, \tag{23}$$

where L_i and L_j are the losses associated with destruction of the objects B_i and B_j, P_{ij} is the annual probability of a collision between the objects B_i and B_j, P_c is the annual probability of a catastrophic collision (1), and P_k is the the annual probability (2) of a collision involving the object B_k. If an object B_k maneuvers to avoid tracked objects, the corresponding value P_k can be set to 0.

A comprehensive database of operational satellites can be found online [7], but the costs of the assets are not readily available, and we will assume that they are roughly proportional to the mass of the asset,

$$L_k = \alpha_k M_k. \tag{24}$$

According to a study conducted by the Aerospace Corporation [8], the cost of developing and building satellites ranges from \$100K/kg to \$900K/kg. We should add launch costs, and also account for investment losses and financial losses resulting from the loss of data and functionality and service interruptions in case of a collision. If we use a conservative estimate of $\alpha_k \sim$ \$150K/kg in formula (24), and assume that the high value assets are successfully avoiding all tracked objects, and that satellites in constellations actively avoid each other, the average immediate loss will be on the order of \$30M. This amount is comparable with the loss in the Cosmos-Iridium collision.

The above calculation assumes that dead satellites and upper stages have no value ($\alpha_k = 0$). This may not be the case. The authors have argued recently [9] that these objects may be used as a source of materials. It took a lot of money to put them in orbit, and they still carry some residual value. For example, there are about 1,000 tons of mostly aluminum in the upper stages alone, and it would take \$5–10B and many years to launch this amount of metal into orbit. The real cost of this "scrap metal" cannot be fully discovered until (and unless) the market develops, but there is a logical range for it. On the one hand, the cost per kilogram must be much lower than the launch costs to create demand. On the other hand, it must be substantially higher than the cheapest delivery cost to create supply. The cost of delivery with electrodynamic vehicles has been estimated at ~\$400/kg [3]. With the current launch prices, a rate of $\alpha_k \sim$ \$1K/kg may drive both the supply and demand sides of in-orbit recycling. At this rate, on the order of \$3M of potentially recyclable materials will be lost on average in a catastrophic collision.

These amounts pale in comparison with the amount of the post-collision (delayed) damage. To evaluate the statistically expected delayed damage to the assets

A_n from the fragments produced in a catastrophic collision, we need to specify their loss functions. A hit by a relatively large fragment within the body area will typically result in a total loss, while a hit by a relatively small fragment may cause only minor damage. Fragments of intermediate sizes may disable some components, but not cause a total loss. To quantify partial losses for the assets A_n, we introduce loss functions $\zeta_n(m)$ depending on the mass of the fragments, such that $0 \leqslant \zeta_n \leqslant 1$ and $d\zeta_n/dm \geqslant 0$ (Fig. 7). They represent statistical averages over all possible hits by fragments of a given mass.

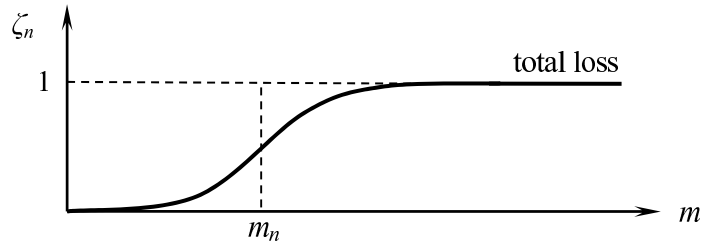

Fig. 7. Typical loss function.

We will also account for the depreciation of the asset values with time by introducing depreciation coefficients $\eta_n(t)$, such that $\eta_n(0) = 1$ and $d\eta_n/dt < 0$. Then, an average statistically expected damage from a hit of a fragment of mass m at time t after the collision can be expressed as

$$d_n(m,t) = L_n\,\zeta_n(m)\,\eta_n(t), \tag{25}$$

where L_n is the amount of a total loss. Using formulas (22) and (25), the average statistically expected damage to the asset A_n over its lifetime T_n caused by the collision fragments can be evaluated as

$$D_n = \int_0^{T_n} \eta_n(t)\,dt \int_0^{\infty} L_n\zeta_n(m)\,\sigma_n\Psi_n\,dm, \tag{26}$$

where σ_n is the average collision cross-section area of the asset A_n, and the flux density Ψ_n is defined by (22) at the average altitude H_n of the asset A_n, assuming that the eccentricity of its orbit is relatively small. Note that the sum in Ψ_n should not include terms associated with the asset itself, because the asset cannot be hit by its own future fragments.

With exponential depreciation $\eta_n(t) = e^{-\chi_n t}$, and the power law distribution (10) of the fragments by mass, formula (26) is reduced to

$$D_n = L_n T_n q_n \sigma_n \Phi_n, \tag{27}$$

where the average depreciation coefficient

$$q_n = (\eta_n^* - 1)/\ln\eta_n^* \tag{28}$$

is expressed through the end-of-life value $\eta_n^* = \eta_n(T_n)$, and Φ_n is calculated at the effective "lethality threshold" m_n determined from the following relation

$$\int_0^\infty \zeta_n(m)\,\frac{\gamma\,dm}{m^{1+\gamma}} = m_n^{-\gamma}. \tag{29}$$

The threshold m_n is shown by the dashed line in Fig. 7.

In our estimates, we will assume that the threshold mass m_n can be related to the mass of the asset as

$$m_n \approx \varepsilon_n M_n^\delta m_c^{1-\delta}, \tag{30}$$

with typical values of $\varepsilon_n \sim 10^{-3}$, $\delta \approx 0.5$, and $m_c = 1$ g. This would mean, for example, that a 1-ton satellite can sustain serious damage from a 1-g debris fragment. Keep in mind that relative velocities in LEO can reach 15 km/s, and hits by even small fragments can be very destructive.

The total statistically expected delayed damage to all assets in LEO resulting from a catastrophic collision

$$D_c = \sum_n D_n \tag{31}$$

is estimated to be on the order of \$200M, assuming $\alpha_n \sim$ \$150K/kg in formula (24). A substantial fraction of this damage will come from impacts on high-value assets, not only because they are expensive, but also large.

6. Persistence of small fragments

Once created, the fragments could persist for a long time. Let us consider a model problem of the long-term evolution of a population of fragments with equal ballistic coefficients. We will assume for simplicity that the fragments are in nearly circular orbits. Their orbital decay can be described by the following equation

$$\dot{H} = -\lambda\,\rho_a(H), \tag{32}$$

where H is the average altitude, dot represents differentiation with respect to time, $\lambda = b_c v R$, b_c is the ballistic coefficient, v is the orbital velocity, R is the orbit radius, and $\rho_a(H)$ is the average air density at the altitude H. With the focus on long-term evolution, we will use multi-year averages for the air density.

A single solution $H = H(t)$ of equation (32) over the range of altitudes of interest will define the evolution of the entire population. Let us consider two points of this solution, $H_1 = H(t_1)$ and $H_2 = H(t_2)$, $t_1 < t_2$. In time $t = t_2 - t_1$, the fragments from the altitude H_1 will move to the altitude H_2, and the fragments from the altitude $H_1 + dH_1$ will move to the altitude $H_2 + dH_2$, where

$$dH_2/\dot{H}_2 = dH_1/\dot{H}_1, \tag{33}$$

and $\dot{H}_1$ and $\dot{H}_2$ are the decay rates at the altitudes H_1 and H_2 according to (32). As all fragments from the layer dH_1 move to the layer dH_2, the average spatial density of fragments changes from n_1 to n_2, conserving the total number of fragments,

$$n_1 dH_1 4\pi R_1^2 = n_2 dH_2\, 4\pi R_2^2. \tag{34}$$

Taking into account (33), relation (34) translates into a curious "time-delayed" form of the continuity equation for the vertical flow of fragments,

$$n_1 \dot{H}_1 R_1^2 = n_2 \dot{H}_2 R_2^2. \tag{35}$$

If we disregard the change in the orbit radius compared to the change in the air density, we will arrive at a remarkably simple relation describing the long-term evolution of the fragment density,

$$n_1 \rho_a(H_1) \approx n_2 \rho_a(H_2). \tag{36}$$

For practical calculations, it is easier to integrate (32) backward in time, or use a "reverse" equation

$$\dot{H} = \lambda\, \rho_a(H). \tag{37}$$

Now, we can calculate the density n at any altitude H and time t as

$$n(H,t) \approx n(H_t, 0)\, \rho_a(H_t)/\rho_a(H), \tag{38}$$

where H_t is the altitude reached at time t along the solution of equation (37) with the initial altitude H, and $n(H_t, 0)$ is the initial density at the altitude H_t at time $t = 0$. A typical solution of equation (37) for small fragments with $b_c \sim 0.5$ m^2/kg is plotted in Fig. 8.

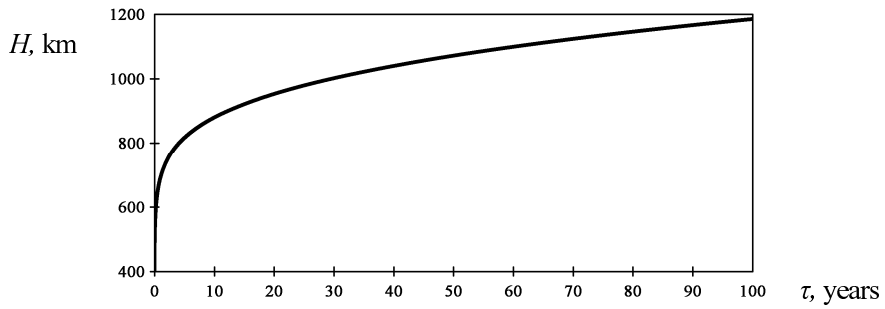

Fig. 8. A typical altitude function for small fragments.

For an exponential air density profile with a constant scale height H_a, it can be expressed as

$$H_t = H + H_a \ln(1 + \lambda t\, \rho_a(H)/H_a), \tag{39}$$

if we disregard the variation of λ with the altitude. Then, relation (38) takes the form

$$n(H,t) \approx \frac{n(H_t,0)}{1 + \lambda t\, \rho_a(H)/H_a}. \tag{40}$$

Even though it was derived for a constant scale height, formula (40) provides a fairly good approximation for the evolution in the atmosphere with a variable scale height. The value H_a in formula (40) can be taken at the altitude H, or as an average between the values at the altitude H and the altitude H_t for better approximation.

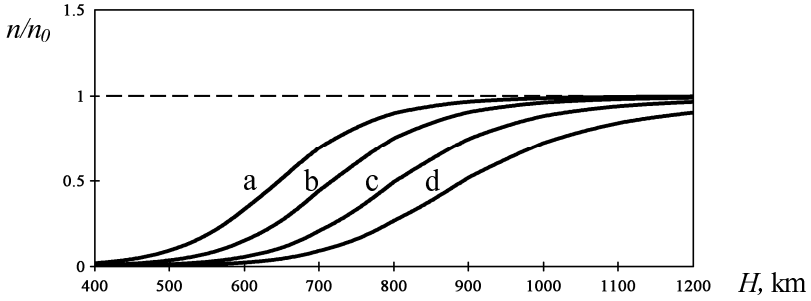

Fig. 9. Sample density profiles for small fragments in a) 1 year, b) 3 years, c) 10 years, d) 30 years.

Fig. 9 illustrates the evolution of a constant initial profile $n(H,0) \equiv n_0$ for small fragments with $b_c \sim 0.5$ m^2/kg. We see that they can persist for a really long time near and above the peak of their production shown in Fig. 6.

Formulas (38) and (40) can be applied directly to sub-populations of fragments with different ballistic coefficients in the virtual stream (17). However, we would like to look at the overall trend from another point of view. Considering all realizations of the succession of collisions in time, we find that the density of the average virtual stream of collision fragments grows as

$$\rho_\tau = \tau\, U(m,H), \tag{41}$$

where τ is time in years, and the annual production rate U is derived from (17),

$$U(m,H) = \sum_{k,i} P_{ki}\, f_{ki}(m)\, g_{ki}(H). \tag{42}$$

The average time in years between catastrophic collisions is equal to $\tau_c = 1/P_c$, where P_c is the annual probability of a catastrophic collision (1). At $\tau =$

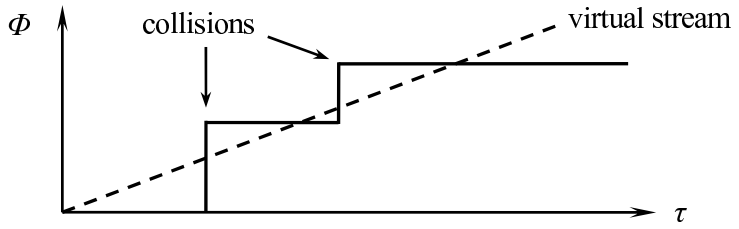

Fig. 10. The virtual stream and collision events.

τ_c, formula (41) turns into (17), as expected, because it reflects accumulation of the collision probability with time. Fig. 10 illustrates the relation between the growth of the average virtual stream (41) and a particular realization of the collision process. Virtual streams can also be evaluated as averages of many simulation runs in numerical models of the debris environment [1,2,10].

According to formula (41), the fragments in the average virtual stream are produced at a constant rate (42). In a small period of time $d\tau$, the fragment density is increased by $d\rho = U d\tau$. Once created, the fragments start migrating down at the rates proportional to the air density at their altitudes. After time τ at an altitude H, we will see fragments from all layers between H and H_τ, where H_τ is defined by the solution of equation (37) with the initial altitude H. Taking into account the density scaling rule (35) and disregarding the radius variation between the layers, we find that

$$\rho_\tau(m,H) \approx \int_0^\tau \frac{\dot{H}_t}{\dot{H}}\, U(m,H_t)\, d\tilde{t} = \frac{1}{\lambda t_y \rho_a(H)} \int_H^{H_\tau} U(m,h)\, dh, \tag{43}$$

where $\tilde{t} = t/t_y$ is time in years, and t_y is a period of one year. Integration yields

$$\rho_\tau \approx \frac{1}{\lambda t_y \rho_a(H)} \sum_{k,i} P_{ki}\, f_{ki}(m)\, [G_{ki}(H) - G_{ki}(H_\tau)], \tag{44}$$

where $G_{ki}(H)$ is the cumulative distribution by altitude (9), which can be applied in a particular form of (15).

Transitioning to the average flux, as we transitioned from (17) to (21), we derive the following formula for the average virtual flux of fragments heavier than m, adjusted for the orbital decay due to air drag,

$$\Phi_n \approx \frac{k_n}{\lambda t_y \rho_a(H)} \sum_{k,i} \beta_{nk}\, P_{ki}\, F_{ki}(m)\, [G_{ki}(H) - G_{ki}(H_\tau)], \tag{45}$$

where the coefficient k_n has the same meaning as in formula (21).

To account for the variability of the ballistic coefficients of the fragments [11], we use a statistical average

$$\Phi_a = \int_0^\infty \Phi_n\, n(b_c)\, db_c, \tag{46}$$

where $n(b_c)$ is a statistically expected distribution of the ballistic coefficients b_c of the fragments in the narrow range of masses around m_c normalized as

$$\int_0^\infty n(b_c)\, db_c = 1.$$

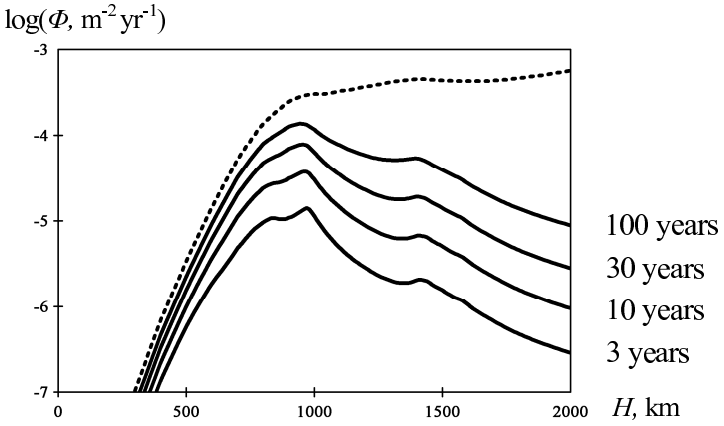

Fig. 11. Growth of the virtual flux of fragments over 1 g.

Fig. 11 illustrates the growth of the average virtual flux encountered by sun-sync assets with the accumulation of collision fragments over 1 g, taking into account their orbital decay due to air drag. These multi-year projections merely illustrate the current trend, they do not predict the future. We see that the accumulation near and above the peak of production will not be reduced much by air drag, while the ISS altitudes will not see high accumulation because the fragments will pass through quickly. The altitude profiles shown in Fig. 11 are similar to the profiles predicted by the debris evolution models [1, 10].

Even though this model is not intended for century-long projections, it captures the fact that the accumulating flux will be evolving toward a balance between the production and the decay of collision fragments (dashed line in Fig. 11), as the contribution of the terms $G_{ki}(H_\tau)$ in (44)–(45) becomes smaller and smaller.

Similarly to formulas (21)–(22), fairly accurate approximations for (44)–(45) can be obtained by replacing the weighted distributions (15) with the base distributions (16) centered around the middle of the altitude overlap.

7. Effectiveness of debris removal campaigns

The model described in this paper can be used to evaluate the effectiveness of various debris removal campaigns. A simple way is to look at the average statistically expected yield of fragments in terms of mass (3) and plan for the maximum reduction of the corresponding annual yield $M_f P_c$ with given campaign resources.

From this standpoint, the remove-first list should include objects with high values of $M_k P_k$, where M_k is the mass of the object B_k, and P_k is the annual probability (2) of a catastrophic collision involving this object.

A formula similar to (3) can be derived for the average number of fragments heavier than $m_c = 1$ g statistically expected to be produced in a catastrophic collision,

$$N_f = \frac{1}{P_c} \sum_{i<j} (\varkappa_{ij} M_i + \varkappa_{ji} M_j)\, P_{ij} = \frac{1}{P_c} \sum_k \varkappa_k M_k\, P_k, \tag{47}$$

where P_c is the annual probability of a catastrophic collision (1), $\varkappa_k$ is the average yield of fragments per unit mass of the object B_k,

$$\varkappa_k = \frac{1}{P_k} \sum_i \varkappa_{ki}\, P_{ki}, \tag{48}$$

P_{ki} are the annual probabilities of a collision between the objects B_k and B_i, and the specific yields $\varkappa_{ki}$ are defined in (10). The corresponding annual yield is $N_f P_c$. According to (47), objects with high values of $\varkappa_k M_k P_k$ should be considered for early removal or collection.

Formulas (21) and (45) further reveal the importance of the "inclination pairing" characterized by the coefficients β_{nk} from (20). In order to reduce the future threat to the most popular orbits, such as the sun-sync orbits, we would need to remove objects with high values of $\beta_{nk} \varkappa_k M_k P_k$, where the coefficients β_{nk} are computed for those particular inclinations.

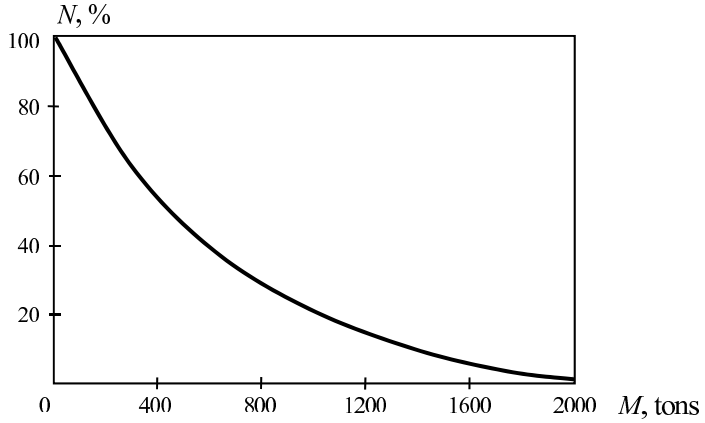

Fig. 12. Reduction of the number of future collision fragments with removal of large debris objects.

Fig. 12 illustrates how the number of small fragments heavier than 1 g produced in catastrophic collisions and accumulated in LEO over the next 50 years can be reduced by removing large debris objects now. The projections are based

on formulas (44)–(45), accounting for the population decay due to air drag. We see that only removal of hundreds of tons of large debris can radically change the future situation in LEO. This is true whether we use formulas (17), (21), (44)–(45), or (47) for the evaluation.

The analysis of the contributions of various sub-populations of large debris objects suggests that the cleanup efforts should focus on the 71–74°, 81–83°, and sun-sync clusters (see also [3]). Removing all rocket bodies from these clusters could reduce the future growth of the population and fluxes of small but potentially lethal debris fragments by a factor of four.

8. Modeling catastrophic collisions

The model described earlier does not assume any particular fragmentation mechanisms, but we would like to share some observations that may be useful in collision fragmentation modeling.

It may seem puzzling at first that the streams of fragments produced in the Cosmos-Iridium collision were tightly focused around the original trajectories of the satellites. It was as if the satellites passed through each other while breaking up. The reason becomes clear from studying the collision geometry. Statistically, most collisions between large objects will have large enough offsets that only modest parts of each object will try to pass through each other directly. For example, same-size circles will have a median overlap of only 18% of the area of each circle. With spheres, the median volume overlap is only 11%. With same-size squares at random angles, the median area overlap is less than 10%, and the median volume overlap for collisions of equal-size cubes is even lower. With similar but not identical sizes, the numbers become lower for the large object and higher for the small one, until a limit is reached, where most collisions fully involve the smaller object.

Masses colliding at up to 15 km/sec create pressures and pressure gradients so large that even solid metals become very compressible. Compression may cause enough adiabatic heating to melt the material, but this may be mostly reversible, as with gases. Extreme pressures and gradients may let most materials shear nearly freely. Shear causes irreversible heating, but the heating cuts shear strength, so materials might keep shearing without generating much more heat. Eventually directly colliding parts will tear apart into irregular hypervelocity sprays of liquid and re-solidified material.

Hypervelocity tests on the ground show a cloud of tiny particles whose leading edge moves out at velocities 30–50% higher than the impact velocity. Even though the kinetic energy of a typical hypervelocity collision is sufficient to heat, melt, and vaporize materials such as aluminum, most of the energy can be carried away by the kinetic energy of the sprays, without being thermalized. Some mass will be vaporized, but the vapor will expand slower and carry far less momentum and

energy than the splashed solid or liquid. The greater mass, speed, and the irregular distribution of splashed mass should make it much more effective at shredding the parts that missed direct impact. Such shredding may create substantially more small shrapnel than other fragmentation mechanisms.

Most of the mass of both rocket bodies and satellites is sheet-like, whether it is part of a tank, rocket engine, structure, solar array, radiator, circuit board, or battery. Hypervelocity spray from directly-impacting parts can shred these sheets into random sizes down to a few times the sheet thickness. Two- vs many-layer designs could make rocket shrapnel different from satellite shrapnel. Most such shrapnel may keep its original thickness over much of its area, and the area-to-mass distribution of fragments may be estimated from the bill of materials.

Analysis of the trajectories of tracked fragments shows that they were ejected from the source objects with velocities of a few percent of orbital velocity. Colliding spacecraft are not "bullets in foam" or "crossed pitchforks," and the question is why their fragments departed at relatively low velocities. The characteristic velocity may be determined by the shear strength and toughness of typical aerospace materials. Shredding sheet-like materials with hypervelocity sprays need not transfer much momentum; it simply cuts the sheets, much as a fast-moving knife can cut an apple without affecting its trajectory much.

Livermore Laboratory conducted a simulation of the Cosmos-Iridium collision using a sophisticated hydrodynamic model with close to a million finite elements per satellite [12]. This model, however, did not simulate processes on the sub-centimeter scale and could not capture the formation of fine hypervelocity sprays. It may not be practical to extend the modeling to a sub-millimeter scale for the entire satellite, but there is another approach. It is similar to experiments in particle accelerators. If a target few centimeters in diameter is hit by a centimeter-size projectile at a velocity typical for orbital collisions, the formation of hypervelocity sprays can be observed experimentally and modeled theoretically down to the sub-millimeter level. Shredding by hypervelocity sprays can be observed by placing typical spacecraft parts around the target and simulated by using particle penetration models [13].

9. Conclusions

Catastrophic collisions between the large objects in LEO will produce hundreds of thousands of debris fragments in the centimeter range ("shrapnel"). The fragments of these sizes are currently untracked and impossible to avoid, but they can disable or seriously damage operational satellites. Statistically, the fragment yield of an average catastrophic collision will be comparable to the yield of the Fengyun-1C and Cosmos–Iridium events combined.

To describe future production and accumulation of small collision fragments, the concept of a virtual stream of fragments is introduced. The virtual stream is

synthesized from the probability-weighted and time-averaged streams of all possible catastrophic collisions between intact objects in LEO. It reflects the current trends in terms of the average statistically expected rates of growth of the population of small collision fragments for any given population of intact debris objects in LEO.

The model is calibrated using available data from the Fengyun-1C and Cosmos–Iridium events. With some simplifying assumptions, the model allows analytical evaluation of the average statistically expected damage to operational satellites from future collisions in LEO. Most of the damage will result from impacts of small fragments in the centimeter range over the years after each catastrophic collision. The model also provides analytical criteria for the effectiveness of debris removal campaigns. It shows that only removal of hundreds of large debris objects from the congested regions in LEO can radically change the current trends in the LEO debris environment.

10. Acknowledgments

This work was partially supported by NASA Ames.

References

1. J.-C. Liou, An active debris removal parametric study for LEO environment remediation, Advances in Space Research, v. 47 (2011), pp. 1865-1876.

2. H. Krag and B.B. Virgili, Analyzing the Effect of Environment Remediation, 3rd International Interdisciplinary Congress on Space Debris Remediation, Montreal, Canada, November 11-12, 2011.

3. E. Levin, J. Pearson, and J. Carroll, Wholesale Debris Removal From LEO, Acta Astronautica, v.73, April-May 2012, pp.100-108.

4. W. Ailor, J. Womack, G. Peterson, and E. Murrell, Space Debris And The Cost Of Space Operations, 4th International Association for the Advancement of Space Safety Conference, Huntsville, Alabama, May 19-21, 2010.

5. D.J. Kessler, Derivation of the Collision Probability between Orbiting Objects: The Lifetimes of Jupiter's Outer Moons, Icarus, Vol. 48, pp. 39-48, 1981.

6. J. Carroll, Bounties for Orbital Debris Threat Reduction? NASA-DARPA International Conference on Orbital Debris Removal, Chantilly, VA, December 8-10, 2009.

7. Internet Database of Operational Satellites, http://www.ucsusa.org/satellite_database

8. D.A. Bearden, Small-Satellite Costs, Crosslink, Winter 2001.

9. J. Pearson, J. Carroll, E. Levin, J. Oldson, ElectroDynamic Debris Eliminator (EDDE) opens LEO for aluminum recovery and reuse, in: 14th Space Manufacturing Conference, NASA Ames, Sunnyvale, CA, October 30-31, 2010.

10. H. Klinkrad, Space Debris: Models and Risk Analysis, Springer, 2006.

11. C. Pardini and L. Anselmo, Physical properties and long-term evolution of the debris clouds produced by two catastrophic collisions in Earth orbit, Advances in Space Research, v. 48, Issue 3, 2011, pp.557569.

12. H.K. Springer, W.O. Miller, J.L. Levatin, A.J. Pertica, S.S. Olivier, Satellite Collision Modeling with Physics-Based Hydrocodes: Debris Generation Predictions of the Iridium-Cosmos Collision Event and Other Impact Events, 2010 AMOS Conference Proceedings, September 14-17, 2010, pp. 362-372.

13. F. Plassard, J. Mespoulet, P. Hereil, Hypervelocity impact of aluminium sphere against aluminium plate: experiment and LS-DYNA correlation, 8th European LS-DYNA Users Conference, Strasbourg, May 2011.

14. G. Stansbery, M. Matney, J.C. Liou, and D. Whitlock, A Comparison of Catastrophic On-Orbit Collisions, 2008 AMOS Conference, September 17-19, 2008.

15. M. Matney, Small Debris Observations from the Iridium 33/Cosmos 2251 Collision, Orbital Debris, Quarterly News, NASA, April 2010.

16. D.J. Kessler and P.D. Anz-Meador, Critical number of spacecraft in low Earth orbit: using satellite fragmentation data to evaluate the stability of the orbital debris environment, in: Proceedings of the Third European Conference on Space Debris, 19-21 March 2001, Darmstadt, Germany, pp.265-272.

17. P.H. Krisko, M. Horstman, and M.L. Fudge, SOCIT4 collisional-breakup test data analysis: With shape and materials characterization, Advances in Space Research, v.41 (2008) 11381146.

18. G.H. Canavan, Analysis of hypervelocity impact test data, Los Alamos National Laboratory, January 1998.

19. T. Hanada and J.-C. Liou, Theoretical and empirical analysis of the average cross-sectional areas of breakup fragments, Advances in Space Research, v.47, Issue 9, 2011, pp. 1480-1489.

20. T. Wang, Technical Research on Space Debris and Other Risks to Spacecraft and Satellites, Beihang University, Report to the MacArthur Foundation, Grant 05-85102-000-GSS, 2009.

21. D.J. Kessler and B.G. Cour-Palais, Collision Frequency of Artificial Satellites: The Creation of a Debris Belt, Journal of Geophysical Research, Vol. 83, No. A6, pp. 2637-2646, June 1, 1978.

22. M. Oswald et al., Upgrade of the MASTER Model, ESA, Final report, April 26, 2006.

23. D. Finkleman and D.L. Oltrogge, The Spectrum of Satellite Breakup and Fragmentation, 2009 AMOS Conference, September 1-4, 2009.

Appendix A
COLLISION PROBABILITY CALCULATION

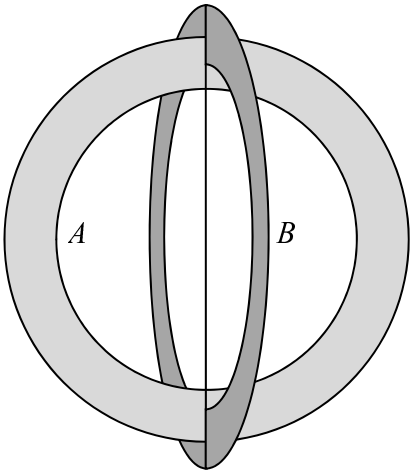

Fig. A1. Intersection of the orbital disc areas.

Let us consider two objects A and B in precessing Keplerian orbits with relatively small eccentricities. The semi-major axes, eccentricities and inclinations are assumed fixed, but other parameters are random. In the multitude of all possible realizations, the trajectories fill the disc areas between the perigee and the apogee, while the disks assume different orientations through their rotation about the Earth's axis. The sweep of the phase space is achieved through random initial conditions, apsidal precession, and nodal regression.

If the discs intersect, as shown in Fig. A1, collision is possible at the intersection line. Object A crosses the intersection line twice per orbit, or

$$N_y = \frac{t_y}{\pi/\omega} = \frac{\omega t_y}{\pi} \tag{A1}$$

times per year, where t_y is a period of one year, and ω is the mean orbital rate.

With random phasing, the probability of crossing the intersection line between altitudes h and $h + dh$ is derived from the laws of Keplerian motion as

$$P_A(h)\, dh \approx \frac{dh}{\pi\sqrt{(H_a - h)(h - H_p)}}, \tag{A2}$$

where H_a is the apogee and H_p is the perigee altitude. Object B has a similar probability distribution $P_B(h)$ with its own apogee and perigee altitudes.

The conditional probability that the two objects will be within "touching distance" in the direction of the intersection line is obtained by integration

$$P_r \approx \int_{H_1}^{H_2} P_A(h)\, P_B(h)\, (D_1 + D_2)\, dh, \tag{A3}$$

where D_1 and D_2 are the typical dimensions of the objects, and (H_1, H_2) is the range of overlapping altitudes.

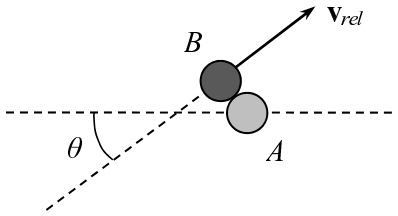

Fig. A2. Relative motion near the intersection.

The conditional probability that the two objects will be within "touching distance" in projection onto a reference sphere near the intersection line with given positions of the ascending nodes of the orbits is approximated as

$$P_\vartheta \approx \frac{D_1 + D_2}{2\pi R \sin\vartheta}, \tag{A4}$$

where R is the average orbit radius, and ϑ is the angle between the tangent to the trajectory of the object A and the velocity of the object B relative to the object A near the intersection, as shown in Fig. A2. The reasoning is very simple. When the center of the object B passes the intersection line, the distance between the center of the object A and the intersection line measured along the orbit of the object A can be anywhere between 0 and approximately πR, but a collision can occur only when the distance is less than $(D_1 + D_2)/2 \sin\vartheta$.

If the objects maintain certain attitude, their dimensions in formulas (A1) and (A4) could have more specific meaning. For example, if we consider two gravitationally stabilized cylinders, the dimensions in formula (A1) will represents their heights, while the dimensions in formula (A4) will represents their diameters.

Averaging over all possible nodal positions yields

$$P_\vartheta \approx \frac{D_1 + D_2}{2\pi R}\, \beta, \tag{A5}$$

where β is the "inclination pairing" coefficient, as defined by Carroll [6],

$$\beta = \frac{1}{2\pi} \int_0^{2\pi} \frac{d\varphi}{\sin\vartheta}, \tag{A6}$$

and φ is the ascending node difference between the orbits of the objects A and B. Carroll suggested a good heuristic approximation

$$\beta \approx \frac{\sqrt{1 + (a \ln \eta)^2}}{\cos \delta_1 \cos \delta_2}, \qquad \eta = |\cos(\delta_1 + \delta_2)| + b, \tag{A7}$$

where $a = 0.347$, $b = (D_1 + D_2)/2\pi R + (e_1 + e_2)/4$, $\delta_{1,2} = i_{1,2}/2$, while $i_{1,2}$ and $e_{1,2}$ are the inclinations and the eccentricities of the orbits, $e_{1,2} \ll 1$. The term b eliminates the singularity at $i_1 + i_2 = \pi$. It has little effect on the value of β elsewhere.

The overall probability of collision between the objects A and B in all possible realizations is calculated as

$$P_c \approx P_r \, P_\vartheta \, N_y \tag{A8}$$

per year. This calculation is suitable for statistical "snapshots" and does not take into account orbit evolution due to air drag, solar radiation pressure, and gravitational perturbations other than from J_2.

Appendix B
DISTRIBUTION OF FRAGMENTS BY MASS

The total estimated number of the Fengyun-1C and Cosmos-Iridium fragments left in orbit long enough to be observed can be derived from the NASA data [14,15]. The total mass of the three satellites was 2336 kg. This gives the average yield of fragments per kilogram of the source mass shown in Table B1.

Table B1. Fengyun-1C, Cosmos-2251, and Iridium-33 fragments

Size	Count	Yield
Over ∼0.5 cm	$\sim 1.3 \cdot 10^6$	∼560/kg
Over ∼2 cm	$\sim 1.1 \cdot 10^5$	∼47/kg
Over ∼10 cm	4680	2/kg

Now, we need to estimate the mass distribution, because the fragment mass is the primary factor determining the impact damage to satellites. The fragments smaller than ∼10 cm ("shrapnel") are currently untracked, and their mass-to-area distributions are uncertain. As the tracking capabilities improve, we will know more about the physical properties of the shrapnel, but at this time, we have to base estimates on ground tests and limited orbital data.

For the purpose of future damage assessment, we are most interested in a narrow range between 0.3 and 3 g within the context of a wider range between 0.1 and 50 g. For this range, we will assume a power-law distribution

$$\varkappa_m = \varkappa_c \, (m_c/m)^\gamma, \tag{B1}$$

where $\varkappa_m$ is the yield of fragments with masses larger than m produced on average in a catastrophic collision per unit mass of the source object, m_c is a characteristic mass, $\gamma > 0$ is the exponent, and $\varkappa_c$ is the yield of fragments heavier than m_c.

When $\gamma \neq 1$, the fraction of the total mass of the source object accumulated in orbiting fragments with masses between m_1 and m_2 is calculated as

$$\eta = \int_{\varkappa_2}^{\varkappa_1} m \, d\varkappa_m = \frac{\gamma}{1-\gamma} \, (\varkappa_2 m_2 - \varkappa_1 m_1), \tag{B2}$$

where $\varkappa_{1,2} = \varkappa_m(m_{1,2})$. When $\gamma = 1$, the fraction of mass in this range is equal to

$$\eta_1 = \varkappa_c m_c \ln(m_2/m_1). \tag{B3}$$

For our purposes, we set $m_c = 1$ g, $m_1 = 0.1$ g, and $m_2 = 50$ g.

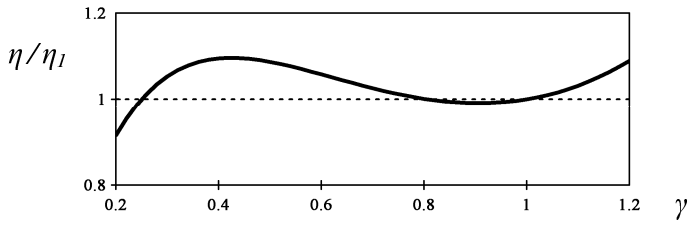

Fig. B1. Variation of the fragment mass fraction with γ.

It turns out that the value of η is not very sensitive to the variation of γ: it remains within 10% of η_1 in a wide range $0.2 < \gamma < 1.2$, as shown in Fig. B1. Therefore, estimates for the yield $\varkappa_c$ and the mass fraction η can be related without knowing the exact exponent γ,

$$\varkappa_c \approx \frac{\eta}{m_c \ln(m_2/m_1)}. \tag{B4}$$

The exponent γ comes into play in the process of "connecting the dots," including the fragment yields by size from Table B1, mass distributions of large tracked fragments, observed mass-to-area distribution patterns, and the total mass of all fragments. The mass distributions for the tracked fragments of Fengyun-1C, Cosmos-2251, and Iridium-33 have not been published at the time of this writing, however, there is a documented mass distribution for the tracked fragments of Solwind (P-78) after its destruction [16]. The mass of this satellite, 878 kg according to [14], was close to the masses of Fengyun-1C and Cosmos-2251. There are also numbers from the series of SOCIT hypervelocity impact tests on the ground [17,18], when a 34.5-kg Navy satellite was destroyed by a projectile moving at 6 km/s. There were other ground tests with much smaller targets and impactors, and much lower velocities [19].

Our analysis and fitting of the published data suggests that the exponent is likely to be close to $\gamma \approx 0.8$, and that around 15% of the source mass ($\eta \approx 0.15$) could be accumulated in fragments between 0.1 and 50 g. This percentage coincides with an estimate for Cosmos-2251 provided in [20]. The corresponding yield of fragments heavier than $m_c = 1$ g will be

$$\varkappa_c \approx 24/\text{kg} \tag{B5}$$

for satellites of this class. This estimate is comparable to the specific yield of fragments derived from the SOCIT test data. It is also consistent with the yields in Table 1, taking into account the mass-to-area distribution patterns observed in the SOCIT tests [17]. We estimate that only a few percent of the source mass may end up in fragments lighter than 0.1 g. Fragments over 50 g carry most of the mass and are usually trackable, but they represent only the "tip of the iceberg" in terms of the number of fragments potentially lethal for operational spacecraft.

To put estimate (B5) in perspective, let us consider a commonly used formula

$$N_m = k\,(M/m)^{\gamma}, \tag{B6}$$

where N_m is the number of fragments heavier than m, and M is the total mass involved in the collision. The original Kessler's formula has $k \approx 0.8$ and $\gamma \approx 0.8$ [21], an early version of the NASA breakup model uses $k \approx 0.45$ and $\gamma \approx 0.75$ [18], the mass distribution of the tracked fragments of Solwind fits $k \approx 0.3$ and $\gamma \approx 0.8$ [16], while the estimate (B5) corresponds to $k \approx 0.4$ and $\gamma \approx 0.8$ for $M \sim 1$ ton. Extended formally toward masses over 10 kg, the estimated distribution converges with the early NASA model. Debris models are evolving [22], and new breakup models are introduced [20, 23]. They will become more accurate when more data on small fragments is gathered.

Appendix C

DISTRIBUTION OF FRAGMENTS BY ALTITUDE

Fig. C1 shows profiles of the altitude residence densities using 1-km bins for the fragments of Fengyun-1C, Cosmos-2251, and Iridium-33 in early 2011. Normalized to the peak value and scaled in altitude, they look strikingly similar. Another known profile for the fragments of the Solwind spacecraft destroyed in 1985 at a substantially lower altitude of 525 km is also very similar [16].

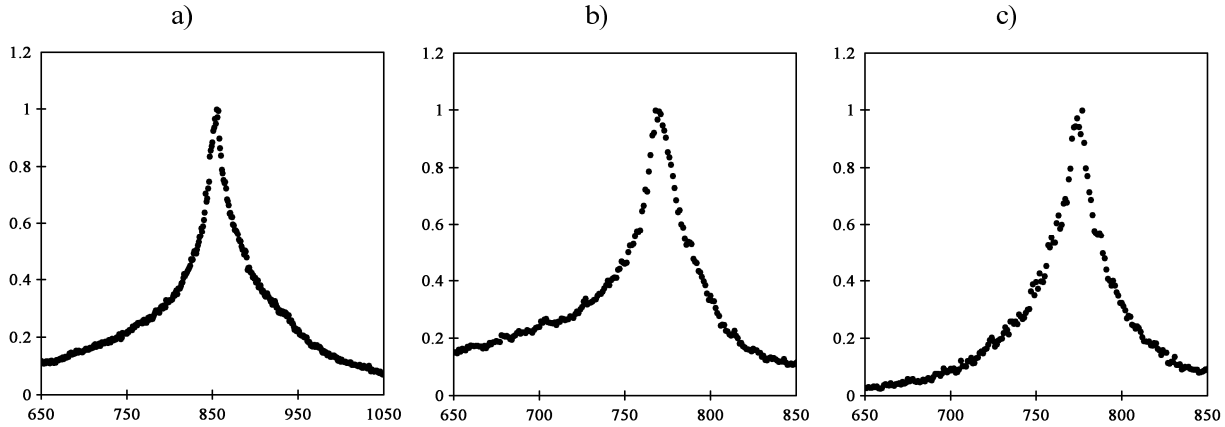

Fig. C1. Altitude densities for fragments of a) Fengyun-1C, b) Cosmos-2251, c) Iridium-33.

Looking at the profiles from these particular events, we want to understand the underlying structure and anticipate a statistically meaningful general pattern that can be used in statistical calculations. Therefore, we will not try to explain the details, but will use very simple approximations instead to capture the trends.

The profiles in Fig. C1 can be roughly approximated by the following formula

$$n(h) = \frac{dN_h}{dh} = \frac{N_f}{h_s} \cdot \frac{k}{(1+a)^b}, \qquad a = \frac{|h-h_0|}{h_s}, \tag{C1}$$

where $n(h)dh$ is the average number of fragments found in the altitude range between h and $h+dh$, N_h is the average number of fragments found below h at any given time, N_f is the total number of fragments, h_0 is the altitude of the peak, h_s is a scale height, $b \approx 2.37$, and $k = (b-1)/2 \approx 0.69$ is a normalization parameter, such that

$$\int_0^\infty n(h)\, dh = N_f. \tag{C2}$$

The scale height h_s is approximately 100 km for Fengyun-1C, 60 km for Cosmos-2251, and 45 km for Iridium-33. The values of b and h_s are not precise and can be floated within certain ranges, which is acceptable for our purposes.

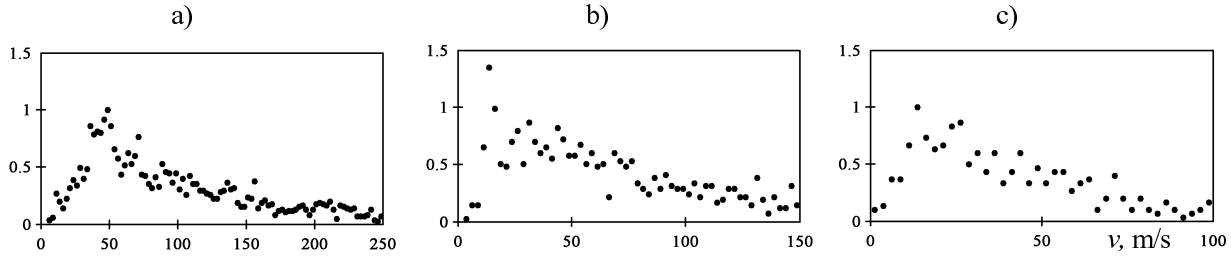

Fig. C2. Velocity distributions for fragments of a) Fengyun-1C, b) Cosmos-2251, c) Iridium-33.

The altitude profiles result from the ejection of the fragments from the collision point. Fig. C2 shows the distributions of the ejection velocities of the fragments of the three satellites using 2.5-m/s bins. These distributions can be roughly approximated by the following formula

$$n(v) = \frac{dN_v}{dv} = \frac{N_f}{v_s} \cdot \frac{ka}{1+a^2}, \qquad a = \left(\frac{v}{v_s}\right)^b, \tag{C3}$$

where $n(v)dv$ is the number of fragments ejected at velocities between v and $v+dv$, N_v is the number of fragments ejected at velocities below v, N_f is the total number of fragments, v_s is a characteristic velocity, $b \approx 1.6$, and $k \approx 0.57$ is a normalization parameter, such that

$$\int_0^\infty n(v)\, dv = N_f. \tag{C4}$$

The characteristic velocity v_s is approximately 50 m/s for Fengyun-1C, 35 m/s for Cosmos-2251, and 20 m/s for Iridium-33. Again, the values of b and v_s are not precise and can be floated within certain ranges.

We note that the scale hight h_s of the altitude density profile and the characteristic ejection velocity v_s are related approximately as

$$h_s \approx 2v_s/\omega, \tag{C5}$$

where ω is an average angular rate of the orbital motion. This is not surprising: faster ejections should result in wider altitude distributions.

The ejection patterns in the observed events were not symmetric. However, when we consider all possible collision conditions, the average ejection pattern should be more symmetric. In a model case of a spherically symmetric ejection from a circular orbit with the velocity distribution (C3), the altitude residence density of the cloud of fragments can be calculated as

$$n(h) = \frac{1}{4\pi} \int_0^\infty n(v)dv \int_{-\pi}^{\pi} d\varphi \int_{-\pi/2}^{\pi/2} \rho(h) \cos\psi \, d\psi \tag{C6}$$

where φ is the angle between the tangent to the orbit and the projection of the ejection direction to the orbital plane, ψ is the angle between the ejection direction and the orbital plane, $\rho(h)$ is the altitude residence density of a fragment moving between the perigee h_p and the apogee h_a of its orbit,

$$\rho(h) \approx \frac{1}{\pi\sqrt{(h_a - h)(h - h_p)}}, \tag{C7}$$

$$h_{a,p} = h_0 + \frac{v}{\omega}\cos\psi\,(2\cos\varphi \pm \sqrt{1 + 3\cos^2\varphi}), \tag{C8}$$

and h_0 is the collision altitude. Fig. C3 shows the velocity distribution (C3) in chart (a) and the altitude profile (C6) in chart (b).

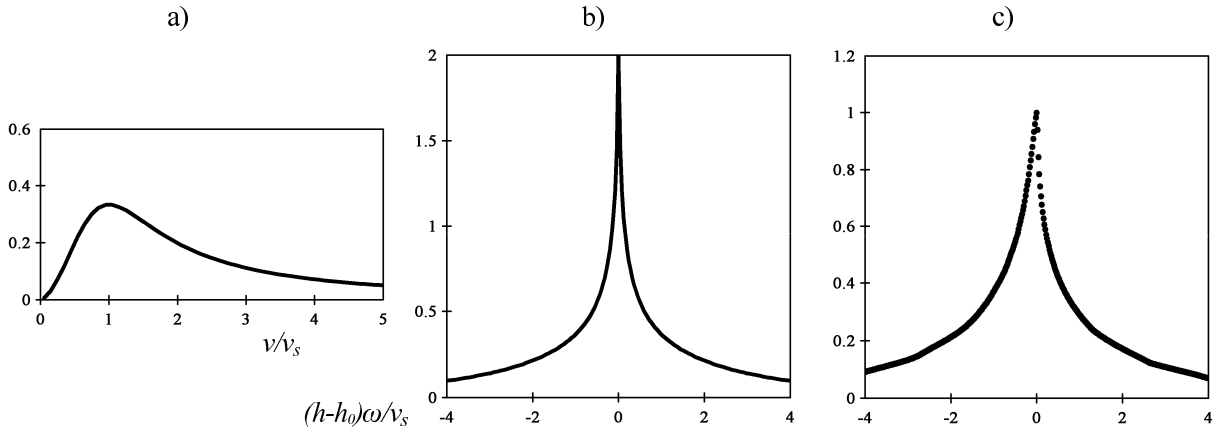

Fig. C3. Spherical ejection: a) velocity profile, b) initial altitude density, c) aged profile.

Mathematically, profile (C6) has a logarithmic singularity at the peak point, however, it is not practically observable in altitude bin counts. Besides, the peak in the initial distribution is quickly diffused by the differential evolution of the orbits of the fragments due to air drag and wide variability of their ballistic coefficients. Aged profiles are calculated by replacing $\rho(h)$ in (C6) with a weighted distribution

$$\tilde{\rho}(h) = \int_0^\infty \rho(h)\, n(b_c)\, db_c, \tag{C9}$$

where $\rho(h)$ is still determined by (C7), but the altitudes of the apogee and perigee are reduced as appropriate for a given ballistic coefficient b_c and a given time after the collision. The average is calculated with a plausible distribution of the ballistic coefficients $n(b_c)$ normalized as

$$\int_0^\infty n(b_c)\, db_c = 1. \tag{C10}$$

Fig. C3 shows a typical aged profile in chart (c), calculated from (C6)–(C10) and normalized to the peak value. It is very similar to the profiles in Fig. C1. Also, the distributions of the inclinations of fragments derived with the above assumptions are consistent with the observed distributions. Therefore, we find these results applicable to statistical calculations.